Spin density in ferromagnetic nickel: a magnetic Compton scattering study

1998 J. Phys.: Condens. Matter 10 2759

(http://iopscience.iop.org/0953-8984/10/12/014)

J. Phys.: Condens. Matter **10** (1998) 2759–2771. Printed in the UK PII: S0953-8984(98)89246-1

Spin density in ferromagnetic nickel: a magnetic Compton scattering study

M A G Dixon†, J A Duffy†, S Gardelis†¶, J E McCarthy†‡, M J Cooper†, S B Dugdale§, T Jarlborg§ and D N Timms‖

† Department of Physics, University of Warwick, Coventry CV4 7AL, UK
‡ ESRF, BP220, F-38043 Grenoble Cédex, France
§ Université de Genève, Département de Physique de la Matière Condensée, 24 quai Ernest Ansermet, CH-1211 Genève 4, Switzerland
‖ Division of Physics, University of Portsmouth, Portsmouth PO1 2DT, UK

Received 14 November 1997

Abstract. The magnetic Compton profiles (MCPs) measured in the [100], [110], [111] and [112] directions in single-crystal nickel with an incident photon beam of energy 224 keV are presented and discussed. The momentum resolution achieved, of 0.43 atomic units, improves on previous studies by almost a factor of two, and facilitates the interpretation of the MCPs in terms of the underlying spin-dependent momentum densities. Calculations have been performed using the linear muffin-tin orbital method, within both the local spin-density approximation (LSDA) and the generalized gradient approximation (GGA). Comparison with experiment reveals the limitations of the LSDA at low momentum, where the GGA is better able to reproduce the contribution of the s- and p-like electrons. All of the calculations overestimate the moment associated with the d-like electrons, for momenta corresponding to the first Brillouin zone. We also confirm the existence of the so-called Umklapp shoulders, which derive from the Fermi surface topology.

1. Introduction

The electronic structure of nickel has been the subject of much theoretical and experimental study. In its ferromagnetic phase, it has a magnetic moment of 0.61 μ_B, of which spin contributes 0.56 μ_B. This net moment is caused by the splitting of the 3d band, and includes the negative polarization of the s- and p-like band electrons (see, for example, [1]). Magnetic Compton scattering, as utilized here, is an ideal experimental technique for investigating the spin moments in such a system.

The electronic and structural properties of Ni and the other magnetic transition metals, Fe and Co, have been used as a testing ground for a number of band-structure calculations within the local spin-density approximation (LSDA) and generalized gradient approximation (GGA). The LSDA is a powerful theoretical tool, but it is unable to account for non-local contributions to the exchange–correlation effects [2]. The GGA modifies the LSDA by adding gradient corrections to the local density model. The most obvious success of the GGA is its ability to predict the correct ferromagnetic phase and bcc structure of Fe, where the LSDA predicts a paramagnetic phase with fcc structure [3, 4]. In

¶ Present address: Cavendish Laboratory, Madingley Road, Cambridge CB3 0HE, UK.

0953-8984/98/122759+13$19.50

Ni, both formalisms are able to predict the correct fcc structure and ferromagnetic phase at room temperature, but the GGA improves the predicted values of the lattice parameter and bulk modulus [5]. Despite these successes, the various formalisms of the GGA have not, in general, improved on the LSDA when applied to calculations of the electronic properties [4, 6]. Considering the linear muffin-tin orbital (LMTO) calculations of Barbiellini *et al* [4], the exchange splitting worsens slightly from 0.7 eV to 0.75 eV, compared to an experimental value of 0.3–0.5 eV [7]. Furthermore, both the LSDA and GGA overestimate the spin moment; the two approximations give the same value, $\mu_{\mathrm{spin}} = 0.62\ \mu_{\mathrm{B}}$, despite the larger exchange splitting predicted by the GGA, because this is compensated by increased negative polarization of the s- and p-like electrons. LMTO calculations were performed within the LSDA and GGA by Ahuja *et al* [6] in order to predict extremal Fermi surface areas in Ni. They calculated a number of such Fermi surface parameters, and found that some changed considerably on using the GGA, worsening the agreement with experimental de Haas–van Alphen data.

The spin-dependent electron momentum density distribution has been calculated using various methods [1, 8–10], although only within the LSDA. It is the one-dimensional (1D) projection of this distribution which can be measured experimentally by Compton scattering, as described in section 2, and magnetic Compton scattering can provide a sensitive method of investigating the spin-dependent properties. Owing to the different characteristic momentum densities of electrons from different bands, it is often possible to separate their relative contributions to the total moment [11]. For example, in Ni, it has already been shown that the negative polarization of the s- and p-like band electrons can be observed [1, 9]. Although the total spin moment is well reproduced by theory, the degree of negative polarization at low momentum, where these electrons contribute, is typically underestimated. This discrepancy is often regarded as being due to the LSDA description of exchange–correlation effects at low momentum [1, 8].

Magnetic Compton profiles (MCPs) have revealed another apparent problem in the theoretical models. The so-called Umklapp features at high momentum, caused by the Fermi surface topology, seem to be much less prominent than predicted. Indeed, in Ni, their existence has been questioned [1, 12], and it has been suggested that this disappearance is also due to electron correlation [13]. It must be stressed, however, that at the resolution available in previous magnetic Compton scattering experiments, such features would have been smeared out. For example, in early experiments on iron with resolutions of 1.0 au [1] and 0.76 au [14], Umklapp shoulders were not observed, but were evident in a more recent experiment, performed at a resolution of 0.42 au [15] (1 au of momentum $= 1.99 \times 10^{-24}$ kg m s^{-1}).

Despite the interest in nickel, and the sensitivity of the magnetic Compton technique to such electronic behaviour, we are unaware of any previously published calculations of the MCPs from Ni using GGA potentials.

In this paper we present new experimental MCPs for Ni, measured on the high-energy x-ray beamline (ID15) at the ESRF. Profiles were measured along four crystallographic directions, [100], [110], [111] and [112], at a much higher resolution than was achieved in previous studies; we obtained a resolution of 0.43 au compared with 1.0 au [1] and 0.7 au [9]. The new information thus obtained undoubtedly leads to a more precise interpretation of the profiles in terms of the underlying spin-dependent electronic structure. In order to perform this interpretation, we have calculated theoretical MCPs using the LMTO method, within both the LSDA and the GGA.

2. Magnetic Compton scattering

Magnetic Compton scattering is now an established technique for probing the spin-dependent momentum densities and band-structures in magnetic materials [13, 16]. It has been shown to be solely sensitive to spin magnetic moments [13, 17, 18] within the impulse approximation [19]; the orbital moment is not measured.

The traditional Compton scattering technique samples a projection of the electron momentum density, where the integrated area under the Compton profile obtained is proportional to the total number of electrons (for further details, see the review by Cooper [20]). A Compton profile is defined as the 1D projection of the electron momentum density, $n(\boldsymbol{p})$,

$$J(p_z) = \int\int n(\boldsymbol{p})\ \mathrm{d}p_x\ \mathrm{d}p_y \tag{1}$$

where p_x, p_y, p_z are the momentum components, with the resolved direction, p_z, parallel to the x-ray scattering vector. The area under the profile equals the number of electrons in the Wigner–Seitz cell, i.e.

$$\int_{-\infty}^{\infty} J(p_z)\ \mathrm{d}p_z = Z. \tag{2}$$

In magnetic Compton scattering, we are interested in those electrons which contribute to the spin moment, and which are, therefore, unpaired. The total electron momentum density can be considered to be composed of spin-up and spin-down band electrons,

$$n(\boldsymbol{p}) = n{\uparrow}(\boldsymbol{p}) + n{\downarrow}(\boldsymbol{p}) \tag{3}$$

where $n\uparrow$ ($n\downarrow$) represents the spin-up (spin-down) band. If a spin moment exists, this is given by the difference in occupancy of the spin-up and spin-down bands, i.e.,

$$\mu_{\mathrm{spin}} = \int [n{\uparrow}(\boldsymbol{p}) - n{\downarrow}(\boldsymbol{p})]\ \mathrm{d}\boldsymbol{p}. \tag{4}$$

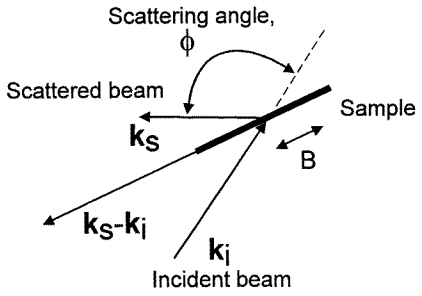

Figure 1. A schematic diagram depicting the scattering geometry adopted in a magnetic Compton scattering experiment. The magnetic field and crystal direction to be measured are aligned with $\boldsymbol{k}_i \cos\phi + \boldsymbol{k}_s$, which is almost coincident with the scattering vector $\boldsymbol{k}_i - \boldsymbol{k}_s$ at high scattering angles. The magnetic field $\boldsymbol{B}$, and hence also the electron spin direction, are reversed by rotating a 1 T magnet.

This difference can be measured in a magnetic Compton experiment due to the spin-dependent terms in the scattering cross-section. There have been numerous derivations of this inelastic scattering cross-section (see [13, 18], for example) which lead to the same

general form, whether free or bound electrons are considered. Here, taking a typical scattering geometry as depicted schematically in figure 1, we follow [21]:

$$\frac{\mathrm{d}^2\sigma}{\mathrm{d}\Omega\ \mathrm{d}E_s} = \frac{r_e^2}{2}\frac{m}{2\hbar K}\left[1+\frac{E_i(1-\cos\phi)}{mc^2}\right]\left(\frac{E_s}{E_i}\right)^2 \times \left\{\left(1+\cos^2\phi + P_l\sin^2\phi + \frac{(E_i-E_s)}{mc^2}(1-\cos\phi)\right)J(p_z) + \left[(\cos\phi-1)P_c\hat{\boldsymbol{\sigma}}\cdot\frac{(\boldsymbol{k}_i\cos\phi+\boldsymbol{k}_s)}{mc}\right]J_{\mathrm{mag}}(p_z)\right\} \tag{5}$$

where r_e is the classical electron radius, P_l and P_c describe the linear and circular polarizations respectively, and $\hat{\boldsymbol{\sigma}}$ is a unit vector parallel to the direction of the sample magnetization. Circularly polarized x-rays are required, since the magnetic term depends on P_c. A reversible magnetic field, applied to the sample, is used to align its magnetic moment alternately parallel and antiparallel to the scattering vector, $\boldsymbol{k}_i\cos\phi+\boldsymbol{k}_s$. This is equivalent to reversing the sign of the $J_{\mathrm{mag}}(p_z)$ term in equation 5. On subtracting the spectra obtained with the two field directions, the charge scattering term cancels and, hence, the magnetic term is isolated. $J_{\mathrm{mag}}(p_z)$ is the spin-dependent momentum density (known as the magnetic Compton profile, MCP):

$$J_{\mathrm{mag}}(p_z) = \int\int (n\uparrow(\boldsymbol{p}) - n\downarrow(\boldsymbol{p}))\ \mathrm{d}p_x\ \mathrm{d}p_y \tag{6}$$

and the area under this profile is equal to the total spin moment per Wigner–Seitz cell:

$$\int_{-\infty}^{\infty} J_{\mathrm{mag}}(p_z)\ \mathrm{d}p_z = \mu_{\mathrm{spin}}. \tag{7}$$

Spin-polarized positron angular correlation experiments also probe the spin density [22], but are subject to positron–electron correlation effects, and repulsion of the positron by the positive ion cores, so the positron does not sample electrons from all states equally [23]. It is this electron–positron momentum distribution, i.e. the electron momentum distribution *as seen by the positron*, that is measured. De Haas–van Alphen measurements are only sensitive to those electrons at the Fermi surface. The value of magnetic Compton scattering stems from its uniform sensitivity to the whole of the electron momentum distribution. Reviews of the technique can be found in [13, 16, 24].

3. Band models of the MCPs

Band-theoretical predictions of the MCPs for Ni have previously been made, within the LSDA, by a number of authors [1, 8–10]. Although we compare various sets of published data, we will concentrate on the FLAPW data of Kubo and Asano [1], and our own LMTO calculations. In this paper, the 3D spin-dependent momentum densities are calculated within both the LSDA and GGA, using the prescriptions of Gunnarsson and Lunqvist [25] and Perdew and Wang [26], respectively. The self-consistent band-structure was calculated at 505 k-points in the irreducible 1/48th part of the Brillouin zone (BZ) using a basis set of s, p, d and f functions. The lattice parameter was set to the experimental room temperature value of 6.6440 au. It is worth noting that the two resultant band-structures are very similar in appearance. The electronic wavefunctions were then used to generate the electron momentum densities for the up- and down-spin bands separately. In the calculation of the momentum density, 893 reciprocal-lattice vectors were used, corresponding to momentum values up to 8.5 au. This momentum density was then projected onto the appropriate

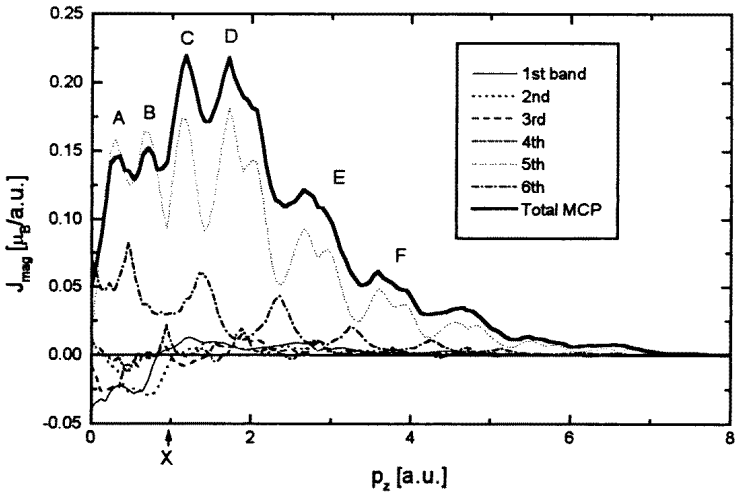

(a)

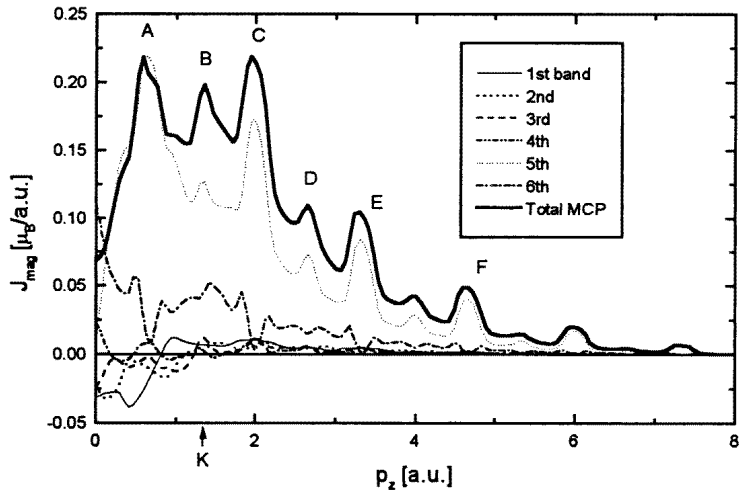

(b)

Figure 2. LMTO-GGA calculation of the magnetic Compton profiles for ferromagnetic nickel; (a) the [100] projection and (b) the [110] projection. The thick solid line represents the total magnetic profile, and the contributions from each band are also indicated. The boundaries of the first Brillouin zones are marked as X and K in (a) and (b) respectively.

crystal directions to produce the Compton profiles, from which the magnetic Compton profiles (shown in figure 2 for two directions) could be constructed. A full description of the technique is given in [4, 27, 28]. The calculated spin moment for both LSDA and GGA was 0.62 μ_B, compared with 0.58 μ_B from the FLAPW-LSDA [1] and an experimental value of 0.56 μ_B. Our results are in agreement with the previously published results of Barbiellini *et al* [4], who used the same LMTO method, but did not calculate the MCPs.

In figure 2, the total MCPs, as well as the contributions from the individual bands, are shown for the [100] and [110] directions, with the position of the first Brillouin zone boundaries marked as X and K respectively. The salient features are:

(i) the negative polarization of the s- and p-like bands (bands 1–4) at low momentum;

(ii) the large dips in the [100] and [110] profiles near $p_z = 0$ au, ascribed partially to the s- and p-like electrons, but also to a pronounced drop in the contribution from the fifth band; and

(iii) the periodic features in the d-like fifth and sixth bands (for example, those labelled A–F), caused by the Fermi surface topology.

For momenta greater than those of the first-Brillouin-zone boundaries, all features are due to Umklapp processes; these are the higher-momentum components of the structures present in the first Brillouin zone. These arise because electrons with a given $\boldsymbol{k}$ contribute to the momentum density at $\boldsymbol{p} = \boldsymbol{k} \pm n\boldsymbol{G}$, where $\boldsymbol{G}$ is the reciprocal-lattice vector, and $n = 0, 1, 2, \ldots$ [23]. The origin of this can be appreciated by considering the momentum density of Bloch electrons

$$n(\boldsymbol{p}) = \sum_{\text{occ}} \sum_{j,k} \left| \int \psi_{j,k}(\boldsymbol{r}) \exp(-\mathrm{i}\boldsymbol{p}\cdot\boldsymbol{r}) \, \mathrm{d}\boldsymbol{r} \right|^2$$
$$= \sum_{j,k,G} \theta(E_f - E_{k,j}) \left| a_{G,j}(\boldsymbol{k}) \right|^2 \delta(\boldsymbol{p} - \boldsymbol{k} - \boldsymbol{G}) \tag{8}$$

where, $\psi_{j,k}(\boldsymbol{r})$ represents the real-space wavefunction for an electron in band j. $\theta(E_f - E_{k,j})$ is the usual step function, i.e. it is unity for $E_{k,j} \leqslant E_f$ and zero otherwise, and is equivalent to the sum over occupied states. The contribution of the higher-momentum components is expressed by the delta function; the intensities of the components are determined by the Fourier coefficients, $a_{G,j}(\boldsymbol{k})$, of the real-space electron wavefunctions. In figure 2 these Umklapp peaks are clearly visible in both [100] and [110] profiles.

4. Experimental details

4.1. The measurement

In this experiment we measured MCPs for four directions in a single crystal of Ni in its ferromagnetic phase, at ambient temperature. The measurements were made at the ESRF using the superconducting wavelength shifter on the high-energy beamline (ID15). The technique is described in [15, 21]. The white beam from this insertion device was monochromated using the 220 reflection of silicon in transmission, the energy selected being 224 keV. Elliptically polarized light was obtained by using only those x-rays emitted at an angle greater than 14 μrad above the orbital plane, resulting in a circular polarization of $\sim$60%. The sample was a 200 μm thick slice, cut perpendicular to [110]. The measurements were made in transmission mode, as depicted in figure 1, and all four projections could be obtained by simply rotating the sample in its plane. The sample was held in a non-magnetic mount in the centre of a rotating permanent 1 T magnet. The scattering angle, ϕ, was 167°. The spectra were collected using a hyperpure germanium solid-state detector, with an energy resolution of $\sim$500 eV at 122 keV. Although this leads to a momentum resolution 2–4 times worse than that obtainable using a scanning crystal spectrometer (see for example [29]), the acquisition of data by the latter is too slow for a systematic investigation. The data for each profile were collected over $\sim$36 hours, giving an integrated count under the Compton profile of 1.3×10^8, which resulted in 8.3×10^5 counts in the MCP. The spectra for each field direction were collected and summed separately. In order to average over any fluctuations in the beam, the magnetic field was flipped every 30 s. Furthermore, the x-ray beam intensity was monitored with a foil-based diode,

in order to facilitate normalization. Any bad data blocks were excluded from the data analysis.

4.2. Data analysis

The data analysis involved in transforming the measured energy spectrum into the magnetic Compton profile has been described previously [16, 21]. The MCP is the difference between two Compton profiles, and this means that the analysis is more straightforward than for the interpretation of a single profile, because the subtraction eliminates some of the possible systematic errors. Corrections for the energy dependence of the x-ray absorption in the sample, the scattering cross-section (in the form given by Bell *et al* [30]) and the detector efficiency were applied. No multiple-scattering correction was made, because estimates [31] show that the magnetic multiple scattering is small ($\sim$1% of the MCP intensity). Whilst the multiple scattering may have an effect on the shape of the MCPs, it will vary smoothly with p_z, and hence none of the interpretation of the data presented in this paper would be affected. Multiple charge scattering, although significant ($\sim$5% of the total intensity), is the same for both spin-up and spin-down data, and hence cancels in the MCP. The resultant magnetic Compton profiles were normalized to the respective calculated magnetic spin moments. Correct normalization of the charge profiles was indicated in the magnetic profiles by (i) the disappearence of fluorescence lines and (ii) the cancellation, within error, of the profiles at high momentum values ($p_z \geqslant 10$ au), where there will be no contribution to the spin density (i.e. spin-up and spin-down profiles are identical). It is clear that MCPs, representing the spin-dependent EMD, will be symmetric, i.e., $J(p_z) = J(-p_z)$. Therefore, in order to improve the statistical accuracy, the profiles were folded about $p_z = 0$ au. Care was taken to ensure that all of the features observed in the folded profiles were indeed real, i.e. appeared at both $+p_z$ and $-p_z$ in the unfolded data sets. Anything that appeared only on one side of the original profile was treated as an artefact, and therefore not considered in any interpretation.

The calculation of the momentum density, using 893 reciprocal-lattice vectors, extends up to 8.5 au. However, there is still a small contribution at momenta higher than this. Inspection of equation (1) shows that, in order to calculate the Compton profile at *any* momentum, the density distribution must be known at all momenta. Fortunately, at high momenta $n(\boldsymbol{p})$, and hence also $J(p_z)$, must approximate to their free-atom values, which have been calculated accurately using the Hartree–Fock method [32]. As a consequence, for the purposes of interpretation, free-atom 3d tails have been added to the theoretical profiles presented in figures 3–5. This correction corresponds to adding a constant of just 0.002 μ_B au^{-1} to the MCPs in the range considered. These profiles were then renormalized to the appropriate calculated moment, as this value is a result of the band-structure calculation.

5. Results

The experimental MCPs for the four high-symmetry directions (filled circles) are presented in figures 3, 4 and 5, together with the LMTO and FLAPW calculations, convoluted with a Gaussian function of full width at half-maximum 0.43 au simulating the experimental resolution. The theoretical MCPs are normalized to their respective calculated moments, and the experiment to the known value of 0.56 μ_B. The theories have not been normalized to this known moment as this corresponds to reducing the exchange splitting, which is

likely to change the shape of the predicted profiles, rather than simply scaling them. The overestimation of the spin moment is a defect of all of the calculations considered.

5.1. The [100] profile

The most obvious feature in the [100] direction (figure 3) is a significant discrepancy between experiment and theory for $p_z < 2$ au. Here, both the LMTO calculations overestimate the moment, and the GGA result is better only below 1 au. Below 1.0 au, none of the calculations are able to predict the depth of the dip in the experimental MCP. Our experimental data are consistent with the earlier results of Sakai *et al* [12] and Timms *et al* [9], where such a dip was also observed, although the feature was less striking due to the poorer resolution of their experiments. Comparison of figure 3 with figure 2(a) reveals a possible source of the disagreement. According to the calculations, the fifth band contains two large peaks labelled A and B, at 0.3 au and 0.7 au. Despite the experimental resolution, which smears the features into one peak (marked A, B), it is clear that a corresponding feature is not observed in the experimental profile. With this in mind, the profile shape in the second Brillouin zone, i.e. for 0.95 au $< p_z <$ 1.90 au, is interesting. Here, two further fifth-band peaks labelled C and D in figure 2(a) are predicted, at 1.25 au and 1.70 au, which are actually Umklapps of the peaks A and B in the first Brillouin zone, i.e. they derive from features in the momentum density propagated by reciprocal-lattice vectors from those in first zone (see equation (8)). However, here the experimental profile follows the FLAPW theory closely; there is a small discrepancy at 1.2 au (C), but the peak at 1.7 au (D) is well reproduced. There is no indication of the difference observed in the first zone. Whilst both LMTO results are too high, their shape is similar to the experimental profile, which clearly is not true for peaks A and B.

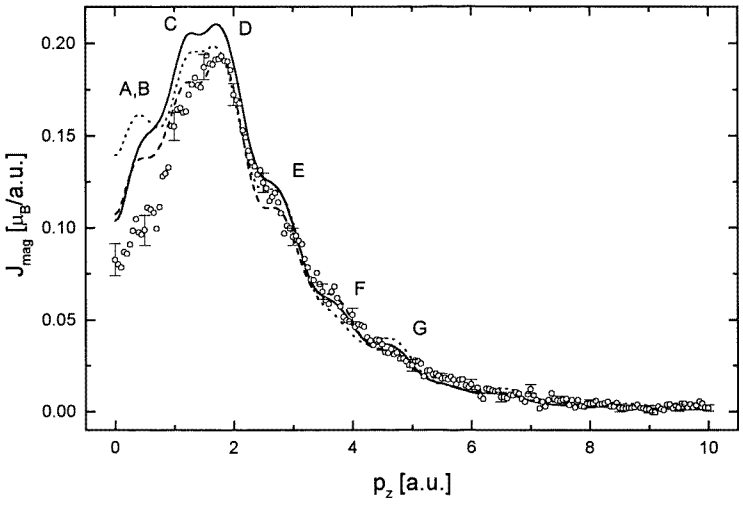

Figure 3. Experimental and theoretical MCPS for nickel [100]. The symbols are as follows: solid line: LMTO-GGA; dotted line: LMTO-LSDA; dashed line: FLAPW-LSDA; circles: experiment. The theoretical profiles have been convoluted with a Gaussian with FWHM = 0.43 au to represent the experimental resolution. The experimental profile has been normalized to a spin moment, $\mu_{\text{spin}} = 0.56\ \mu_{\text{B}}$, the FLAPW to $\mu_{\text{spin}} = 0.58\ \mu_{\text{B}}$, and both LMTO results to $\mu_{\text{spin}} = 0.62\ \mu_{\text{B}}$.

At higher momenta, further Umklapp features can be observed at ∼2.7 au and ∼3.6 au, corresponding to the shoulders E and F in the theoretical profiles. At E, the theories give different predictions for the absolute values of the MCPS, but in all cases the experimental shoulder appears to be smeared in comparison with the calculated profiles. At points F and G the GGA shows an improvement over the LSDA, but, again, the FLAPW is more accurate.

5.2. The [110] profile

Observations of the [110] profile (in figure 4, which are to be compared with the calculated partial profiles in figure 2(b)) are consistent with the situation found for [100]. Here, a first-zone peak at 0.7 au, marked A, and predicted to occur in all theoretical curves, is absent in the experiment, but its Umklapp is observed experimentally (peak C), although the contribution is overestimated. Between 1.0 au and 2.5 au, the FLAPW theory provides the best description of the experimental curve, and the LMTO-GGA calculation gives the worst prediction. However, it should be noted that, despite the differences in the absolute values of $J(p_z)$, all three curves provide a good description of the shape of the profile here. In the inset to figure 4, over a smaller range of momentum, we present the experimental data together with the LMTO-GGA calculation results, with the theory normalized to the experimental moment of 0.56 μ_B. This indicates that the predicted shape of the MCP is in good agreement in this momentum range, except for the peak at A which is still not reproduced. As noted previously, renormalizing the moment is not strictly valid, because its value derives from the exchange splitting and reducing this will not necessarily simply scale the MCP.

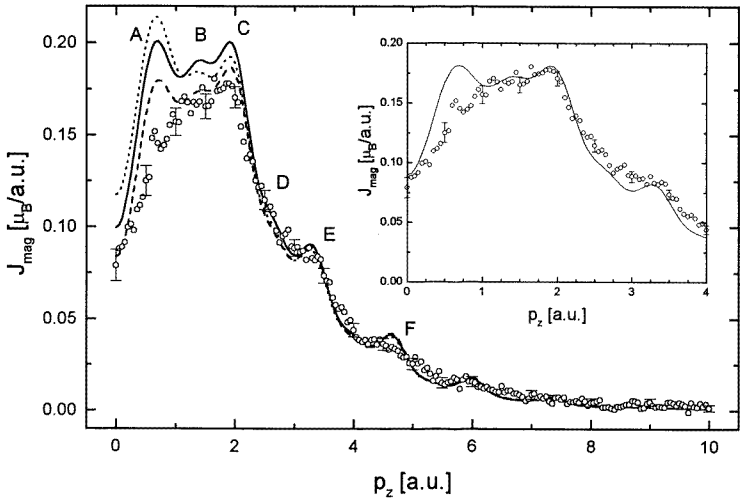

Figure 4. Experimental and theoretical MCPS for nickel [110]. The symbols are as for figure 3. Beyond 3 au, the theoretical MCPs are coincident. The inset shows the experimental and LMTO-GGA theory results, both normalized to the experimental moment of 0.56 μ_B.

At higher momenta, shoulders (E and F) appear at ∼3.3 au and ∼4.7 au which again are less evident than in theory, especially at F. Note that the three theoretical results are in agreement with each other in this momentum region. We have eliminated sample misalignment as a cause of the smearing by simulating this effect: rotating the theoretical momentum density by a few degrees before integrating did not reproduce the observed

blurring. The difference between experiment and theory is too large to be masked by the statistical errors.

In the [110] profile, our data disagree with previous experimental data at a resolution of 1.0 au [12]. However, in the previous results very few features of the line shape are discernible, due to the poorer resolution. It is clear that, in the first Brillouin zone, we observe a larger dip in the magnetic profile than any of the calculations predict. Furthermore, the existence of the Umklapp structures is established in our data by the much improved resolution. Hence, in contrast with previous work [12], this study concludes that electron correlation effects do not eliminate these fine structures. This is consistent with findings for iron where the features were only rendered visible experimentally at a resolution of 0.42 au [15].

5.3. The [111] and [112] profiles

In the [111] profile (figure 5), the LMTO calculations again overestimate $J_{\mathrm{mag}}(p_z)$ at low momentum. The FLAPW calculation reproduces the dip, and the small peak within it (marked A) in the experimental profile, although there is a discrepancy at B. Both LMTO calculations overestimate the size of the low-momentum peak at A, and LCGO [8] and APW [9] calculations fail in a similar manner. Previous experimental data for Ni [9] contained little evidence of this peak and it had been suggested [8] that the LSDA was at fault, rather than the methodology, but this is not borne out by our analysis. However, the previous data [1, 9] were at a resolution where the features would, in any case, be much less evident, especially in view of the masking effects of the statistical noise in those profiles. Here, as for the [100] profile, our experimental data do agree with those of Sakai *et al* [12], but our present experimental data confirm the predicted existence of this low-momentum peak, clearly demonstrating the benefits offered by the improved resolution.

The fourth profile measured, for the [112] direction, also presented in figure 5, exhibits

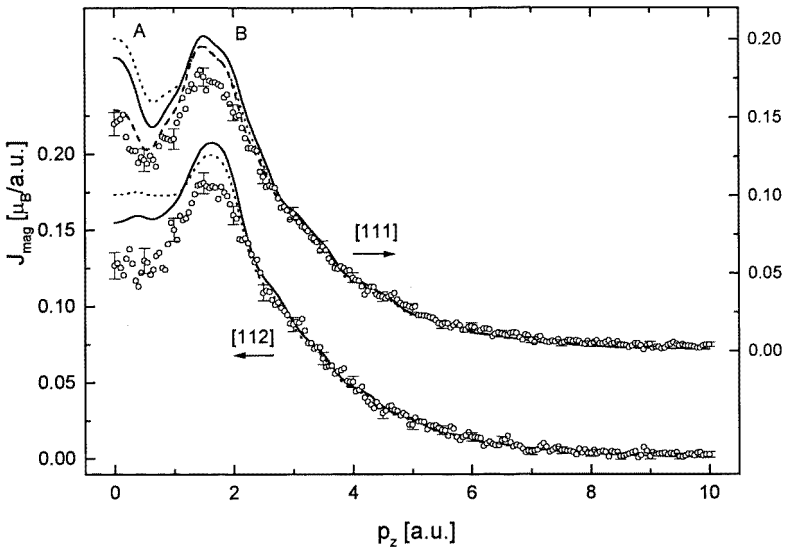

Figure 5. Experimental and theoretical MCPS for nickel [111] and [112]. The symbols are as for figure 3.

the same trends in the LMTO results. The GGA calculation, whilst not providing a good fit to the experimental data, does show improvement over the LSDA below 1.0 au. Here, FLAPW data were unavailable.

5.4. Discussion

In general, the MCPs from the FLAPW-LSDA calculations agree better with the experiment than the LMTO calculation; this is due, in part, to the fact that the FLAPW calculation produces a value for the spin moment closer to the accepted experimental value. Comparison of the two LMTO results does indicate the improvement gained by invoking the GGA. Despite the fact that the calculated value of the spin moment is not improved and, indeed, the exchange splitting and Fermi surface extremal areas are worse [6], the description of the general shape of the magnetic Compton profile, and hence, in principle, the calculated momentum density is improved. This paradox demands further investigation; our observations illustrate that this is not a trivial problem, and it is one which we aim to pursue. However, it is worth noting here that comparison of our LSDA and GGA band-structures does not reveal the large variations in the Fermi surface parameters predicted by the calculations of Ahuja *et al* [6]; we would not conclude from our calculations that these parameters are worse for the GGA. It is interesting that the resultant MCPs (and hence the electron momentum distributions) are significantly different despite the similarity of the band-structures. It would be informative to see whether a GGA full-potential calculation could reduce the remaining discrepancies in the FLAPW-LSDA MCPs, without similarly causing a deterioration in comparisons with the quantities derived directly from the band-structure.

Concentrating in particular on the [100] and the [110] profiles, we believe that a significant part of the observable discrepancy in the predicted profiles may be due to the fifth band, rather than being solely due to the negatively polarized s- and p-like bands previously believed to be responsible [1, 9] for the low-momentum behaviour of the profile. The clear contribution of the fifth band at high momenta, where it dominates the calculated MCPs, leads us to contend that the calculated band-structure (and hence Fermi surface) is not wrong, but that the distribution of the momentum density revealed by this experiment is weighted to higher momenta. However, the treatment of the negatively polarized electrons is also important, as is made apparent by the comparison of the LSDA and GGA. The GGA performs better where these electrons contribute, i.e. below 1.0 au. This corresponds to the larger negative moment of these electrons predicted by the GGA. Hence, we suggest that non-local exchange–correlation effects are significant in nickel, and that these are only dramatically observed at low momentum, i.e., where contributions from the first Brillouin zone dominate.

6. Conclusions

The present experiment demonstrates the benefits of the higher resolution now obtainable by using high-energy circularly polarized photons at the ESRF. The predicted [111] central peak is unambiguously observed for the first time and in the [110] direction there is definite evidence of Umklapp effects, although their prominence is overestimated by the band calculations. For the [100] projection, a much deeper dip than predicted by any of the LSDA techniques is found, and in agreement with [1] our proposal is that this is partly due to the LSDA. Although our LMTO-GGA calculation does not eliminate this discrepancy, it does produce an improvement.

In general, the LMTO technique does not perform as well as the FLAPW, but it is much less intensive in terms of computer time. Although the moment, and hence also the size, of the MCPs is overestimated, the detailed shape is in good agreement with the FLAPW results. It is clear that the main discrepancy in the LMTO results is significant only at low momentum: in each profile the MCP is described well for momenta above 2.5 au. Furthermore, the GGA improves on the LSDA at momenta below 1 au, where the negatively polarized s–p-like electrons contribute. From an experimental point of view, high-resolution measurements ($\Delta \boldsymbol{p} \approx 0.15$ au, achievable with a crystal spectrometer) would now be useful in order to investigate specific features in these profiles which are not well described, i.e. the shapes of the profiles at low momentum and the blurring of the Umklapp features. Unfortunately such a magnetic measurement for Ni would be at the limit of viability with the currently available instruments.

Acknowledgments

We are grateful to the ESRF for the provision of beam-time, and to V Honkimäki, T Tschentscher and P Suortti for technical help. We thank A Manuel and G Santi for invaluable discussions. Thanks are also due to Y Kubo, for sending us his FLAPW data. We thank the EPSRC for financial support and for the provision of a postdoctoral research assistantship (JAD). The project was also supported by the Human Capital and Mobility Programme in the European Union through contract ERCBCHRXC5930135.

References

[1] Kubo Y and Asano S 1990 *Phys. Rev.* B **42** 4431
[2] Perdew J P 1991 *Physica* B **172** 1
[3] Bagno P, Jepsen O and Gunnarsson O 1989 *Phys. Rev.* B **40** 1997
[4] Barbiellini B, Moroni E G and Jarlborg T 1990 *J. Phys.: Condens. Matter* **2** 7597
[5] Leung T C, Chan C T and Harmon B N 1991 *Phys. Rev.* B **44** 2923
[6] Ahuja R, Auluck S and Johansson B 1994 *Phys. Scr.* **50** 573
[7] Lonzarich G G 1980 *Electrons at the Fermi Surface* ed M Springford (Cambridge: Cambridge University Press)
[8] Sundararajan V and Kanhere D G 1991 *J. Phys.: Condens. Matter* **3** 3311
[9] Timms D N, Brahmia A, Cooper M J, Collins S P, Hamouda S, Laundy D, Kilbourne C and Saint Lager M-C 1990 *J. Phys.: Condens. Matter* **2** 3427
[10] Rennert P, Carl G and Hergert W 1983 *Phys. Status Solidi* **120** 273
[11] Lawson P K, Cooper M J, Dixon M A G, Timms D N, Zukowski E, Itoh F and Sakurai H 1997 *Phys. Rev.* B **56** 3239
Cooper M J, Lawson P K, Dixon M A G, Zukowski E, Timms D N, Itoh F, Sakurai H, Kawata H, Tanaka Y and Ito M 1996 *Phys. Rev.* B **54** 4068
[12] Sakai N, Ito M, Kawata H, Iwazumi T, Ando M, Shiotani N, Itoh F, Sakurai Y and Nanao S 1991 *Nucl. Instrum. Methods* A **303** 488
[13] Sakai N 1996 *J. Appl. Crystallogr.* **29** 81
[14] Tanaka Y, Sakai N, Kubo Y and Kawata H 1993 *Phys. Rev. Lett.* **70** 1537
[15] McCarthy J E, Cooper M J, Lawson P K, Timms D N, Manninen S O, Hämäläinen K and Suortti P 1997 *J. Synchrot. Radiat.* **4** 102
[16] Cooper M J 1997 *J. Radiat. Phys. Chem* **50** 63
[17] Cooper M J, Zukowski E, Collins S P, Timms D N, Itoh F and Sakurai H 1992 *J. Phys.: Condens. Matter* **4** L399
[18] Lovesey S W 1996 *J. Phys.: Condens. Matter* **8** L353
[19] Carra P, Fabrizio M, Santoro G and Thole B T 1996 *Phys. Rev.* B **53** R5994
[20] Cooper M J 1985 *Rep. Prog. Phys.* **48** 415

[21] McCarthy J E, Cooper M J, Honkimäki V, Tschentscher T, Suortti P, Gardelis S, Hämäläinen K, Manninen S O and Timms D N 1997 *Nucl. Instrum. Methods* A **401** 463
[22] Genoud P, Manuel A A, Walker E and Peter M 1991 *J. Phys.: Condens. Matter* **3** 4201
[23] West R N 1995 *Proc. Int. 'Enrico Fermi' School of Physics on Positron Spectroscopy of Solids* ed A Dupasquier and A P Mills Jr (Amsterdam: IOS Press)
[24] Lovesey S W and Collins S P 1996 *X-ray Scattering and Absorption by Magnetic Materials* (Oxford: Clarendon)
[25] Gunnarsson O and Lunqvist B I 1976 *Phys. Rev.* B **13** 4274
[26] Perdew J P 1985 *Phys. Rev. Lett.* **55** 1665
Perdew J P and Wang Y 1986 *Phys. Rev.* B **33** 8800
Perdew J P 1986 *Phys. Rev.* B **33** 8822
Perdew J P 1986 *Phys. Rev.* B **34** 7406
[27] Andersen O K 1975 *Phys. Rev.* B **12** 3060
Jarlborg T and Arbman G 1977 *J. Phys. F: Met. Phys.* **7** 1635
[28] Jarlborg T and Singh A K 1985 *J. Phys. F: Met. Phys.* **15** 727
[29] Manninen S, Honkimäki V, Hämäläinen K, Laukkanen J, Blaas C, Redinger J, McCarthy J and Suortti P 1996 *Phys. Rev.* B **53** 7714
[30] Bell F, Felsteiner J and Pitaevskii L P 1996 *Phys. Rev.* A **53** R1213
[31] Sakai N 1987 *J. Phys. Soc. Japan* **56** 2477
[32] Biggs F, Mendelsohn L B and Mann J B 1975 *At. Data Nucl. Data Tables* **16** 201